

Final Draft
of the original manuscript:

Li, B.; Guan, K.; Yang, Q.; Niu, X.; Zhang, D.; Lv, S.; Meng, F.; Huang, Y.; Hort, N.; Meng, J.:

Microstructures and mechanical properties of a hot-extruded Mg–8Gd–3Yb–1.2Zn–0.5Zr (wt%) alloy.

In: Journal of Alloys and Compounds. Vol. 776 (2019) 666 - 678.

First published online by Elsevier: 29.10.2018

DOI: 10.1016/j.jallcom.2018.10.322

<https://dx.doi.org/10.1016/j.jallcom.2018.10.322>

Microstructures and mechanical properties of a hot-extruded Mg-8Gd-3Yb-1.2Zn-0.5Zr (wt.%) alloy

B. Li^{1,4} and K. Guan^{1,4}, Q. Yang¹, X. Niu¹, D. Zhang¹, S. Lv², F. Meng², Y. Huang³, N. Hort³, J. Meng¹

¹State Key Laboratory of Rare Earth Resource Utilization,
Changchun Institute of Applied Chemistry, Chinese Academy of
Sciences, Changchun, 130022, PR China

²School of Materials Science and Engineering, Changchun
University of Science and Technology, 130022, PR China

³Magnesium Innovation Centre, Helmholtz-Zentrum Geesthacht,
Max-Planck-Strasse 1, 21502, Geesthacht, Germany

⁴University of Chinese Academy of Sciences, Beijing, 100049, PR
China

Abstract

Microstructures and mechanical properties of a Mg-8Gd-3Yb-1.2Zn-0.5Zr (wt.%) alloy have been investigated. The dominant intermetallic phases in the as-cast sample are Mg₅RE (RE = Gd, Yb) phase, 14H-type long-period stacking ordered (LPSO) phase, and Mg₂Zn₂RE (W) phase and ordered Mg₁₂RE phase. Furthermore, the ordered Mg₁₂RE phase generally coexists with the W phase following an orientation relationship as $[0\bar{1}1]_w//[2\bar{3}0]Mg_{12}RE$, and $(\bar{1}11)_w//(001)Mg_{12}RE$. After extrusion, the microstructure is consisted of un-recrystallized regions along with a small part of fine dynamically recrystallized (DRXed) regions. Simultaneously, the coarse Mg₅RE, W and Mg₁₂RE particles were disintegrated and mainly distribute at extrusion stringers while the fine LPSO plates mainly distribute in un-recrystallized regions. Moreover, amounts of nanoscale Mg₅RE particles were dynamically precipitated in DRXed regions. Then, the as-extruded Mg-8Gd-3Yb-1.2Zn-0.5Zr alloy exhibits clearly higher strength than the classic rare-earth-containing magnesium alloys with comparative or even much higher rare earth content at both room temperature and high temperatures. The dominant strengthening mechanism was finally revealed as precipitation/dispersion strengthening.

1 Introduction

Magnesium alloys, owing to the low density, easy recycling and high specific strength, offer significant potential for weight reduction in aerospace, automotive and 3C industries [1-4]. To accelerate the wide applications of magnesium alloys, many investigations have been conducted to improve their strength particularly by alloying. Among the various alloying elements, rare earth (RE) elements are reported to be most effective in improving alloys' strength not only at room temperature (RT) but also at elevated temperatures [5-8]. In the past decades, numerous high-strength Mg-RE-based alloys have been developed. As an example, Homma et al. [9] reported a high-strength Mg-10Gd-5.7Y-1.6Zn-0.7Zr (wt.%) alloy, whose ultimate tensile strength (UTS) and yield strength (YS) are 542 MPa and 473 MPa, respectively. Nonetheless, these high-strength alloys ordinarily have relatively high RE content, thus resulted in high cost [10]. Bearing this in mind, an army of researchers developed Mg-RE-based alloys by clearly reducing the RE content [10,11]. Then, a series of Mg-Gd-based high-strength alloys were developed [12,13]. For instance, Xu et al. [13] reported that the Mg-8.2Gd-3.8Y-1.0Zn-0.4Zr alloy prepared by large-strain hot rolling and subsequent ageing process has UTS and YS of approximately 517 MPa and 426 MPa, respectively. To date, investigating the effects of some alloying elements such as Nd, Er, and Ce on microstructures and mechanical properties of Mg-8Gd-based alloy has become the most interesting topic. Additionally, several high-strength alloys have been successfully developed. For example, Zheng et al. [14] developed a high-strength alloy by adding 1 wt.% Er into a Mg-8Gd-0.5Zr (wt.%) alloy, with the RT-strength is over 500 MPa. In our previous work [12], we fabricated a high-strength Mg-8Gd-1.2Zn-0.5Ce-0.5Zr (wt.%) alloy by traditional hot-extrusion. The UTS and YS of such alloy are approximately 461 MPa and 458 MPa, respectively. Therefore, it can be concluded that the lately developed high-strength alloys are mainly based on the Mg-8Gd system and have even higher strength than the traditional Mg-RE-based alloys with much higher RE content [15,16].

As a representative RE element, Yb has promising influence on the performance of magnesium alloys [17-20]. For instance, Yu et al. [18] reported that adding 2.0 wt.% Yb into a wrought Mg-5Zn-0.5Zr (wt.%) alloy has satisfactory grain refinement and strengthening effect. In addition, the addition of Yb into the Mg-5Al alloy can clearly influence the microstructures and improve the alloy's high-temperature strength [20]. However, there is still no open reported literature involving the effects of Yb addition on microstructures and mechanical properties of the Mg-RE-based alloys. Therefore, to develop high-strength alloy, it is very important to investigate the microstructures and mechanical properties of the Yb-modified Mg-8Gd-based alloys.

With respect to the high-strength Mg-8Gd-based alloys, Zn and Zr were frequently adopted. It is well known that Zn additions can significantly reduce the equilibrium solid solubility of RE in magnesium, thus significantly enhancing the ageing response [21,22]. Furthermore, Zn is an essential element for the formation of long-period stacking ordered (LPSO) phase which is exceedingly favorable to increase the alloys' strength. Simultaneously, Zr addition can remarkably refine grains [23,24]. Therefore, an alloy with nominal compositions of Mg-8Gd-3Yb-1.2Zn-0.5Zr (GYZK8310) in wt.% was adopted in this work and fabricated using the conventional hot-extrusion. The microstructures in both as-cast and as-extruded samples were thoroughly examined. Then, the tensile properties of the as-extruded sample were tested at both RT and high temperatures (200, 250 and 300 °C). Finally, the underlying strengthening mechanisms were analyzed and discussed.

2 Experimental procedures

The GYZK8310 alloy was fabricated by electric melting of pure Mg, Zn, Mg-20 wt.% Yb and Mg-30 wt.% Zr master alloys in a steel crucible under the protection of CO₂ + 1.5 vol.% SF₆ mixture gas. The melt was fully stirred for approximately 15 min after its temperature reached to approximately 750 °C, and then kept static for approximately 25 min at this temperature. Afterwards, the melt was gradually cooled down to 710 ± 5 °C in half an hour. Finally, the melt was poured into an iron mold with a diameter of 90 mm and preheated to approximately 280 °C. The chemical compositions of the obtained alloy were examined by an inductivity coupled plasma atomic emission spectroscopy (ICP-AES) as Mg-7.56Gd-2.72Yb-1.18Zn-0.43Zr in wt.%. Before extrusion, the ingots were machined into billets with diameter of 82 mm. After preheated at 320 °C for approximately 2.5 h, the billets were directly extruded at the same temperature with a ram speed of 0.1 mm/s and an extrusion ratio of 7.

Microstructures were examined using optical microscopy (OM, Olympus-GX71), X-ray diffractometer (XRD, Bruker D8 FOCUS) at 40 kV and 40 mA with Cu K α radiation ($\lambda = 0.15406$ nm), scanning electron microscopy (SEM, Hitachi S-4800) under an accelerating voltage of 10 kV, and transmission electron microscopy (TEM, FEI Tecnai G2 F20) equipped with energy-dispersive X-ray spectroscopy (EDS) operating at 200 kV. Specimens for OM and SEM observations were firstly grinded with different grades of SiC papers, then polished with Al₂O₃ suspension, and finally slightly etched by a mixture of 5 ml acetic acid, 5 g picric acid, 10 ml H₂O, and 100 ml ethanol. Thin foils with 3 mm in diameter for TEM observations were mechanically polished to approximately 20 mm and then ion-beam milled using a precision ion polishing system (Gatan 691) with cooling system

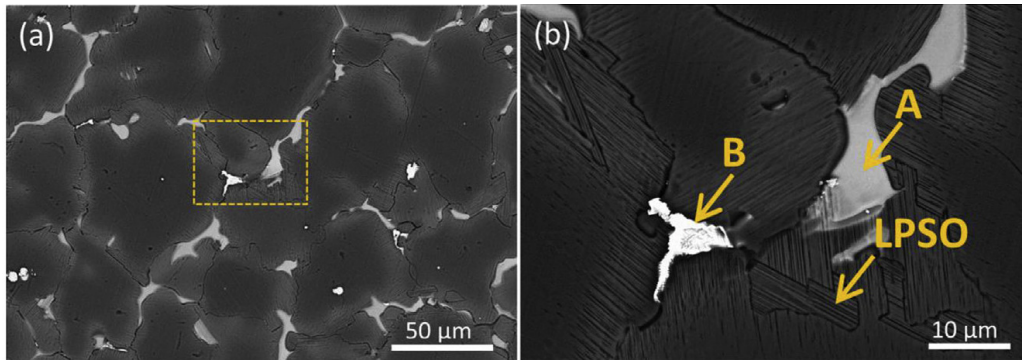


Figure 1: Backscatter SEM micrographs of the as-cast GYZK8310 alloy.

by liquid nitrogen. The grain sizes of the as-cast sample presented in this work were tested using the Nano Measurer software. The texture and the grain size of the as-extruded alloy were examined by an EDAX-TSL electron back-scattered diffraction (EBSD). The samples for EBSD observations were prepared by standard metallographic technique, then polished using 0.08 mm colloidal silica for 20 min, and finally electro-polished at 20 V for approximately 75 s in an AC2 solution at $-5\text{ }^{\circ}\text{C}$. To remove artifacts on the polished surface, samples were sonicated for 25 min after preparation in absolute ethanol.

Cylindrical tensile samples with gauge length and gauge diameter of 36 mm and 6 mm, respectively, were machined from extruded bars with the tensile direction parallel with extrusion direction (ED). Then, tensile tests were carried out on Instron 5869 tension tester with a strain rate of $1.0 \cdot 10^{-3}\text{ s}^{-1}$. Before each high temperature test, a 20 min holding was applied to balance the testing temperature. For each testing condition, at least three effective tests were carried out for every condition to confirm reproducibility and the values presented in this work are the averages.

3 Results and discussion

3.1 Microstructures of the as-cast GYZK8310 alloy

Fig. 1a shows the backscatter SEM image of the as-cast GYZK8310 alloy. The microstructures are mainly composed of α -Mg grains and eutectic phases. The average grain size was measured as $46 \pm 1.6\text{ }\mu\text{m}$. According to Fig. 1b, there are mainly three kinds of intermetallic phases according to morphologies. The brighter phase generally located at triangular grain boundaries (indicated by B) is defined as the blocky phase while the other two phases indicated by A and C,

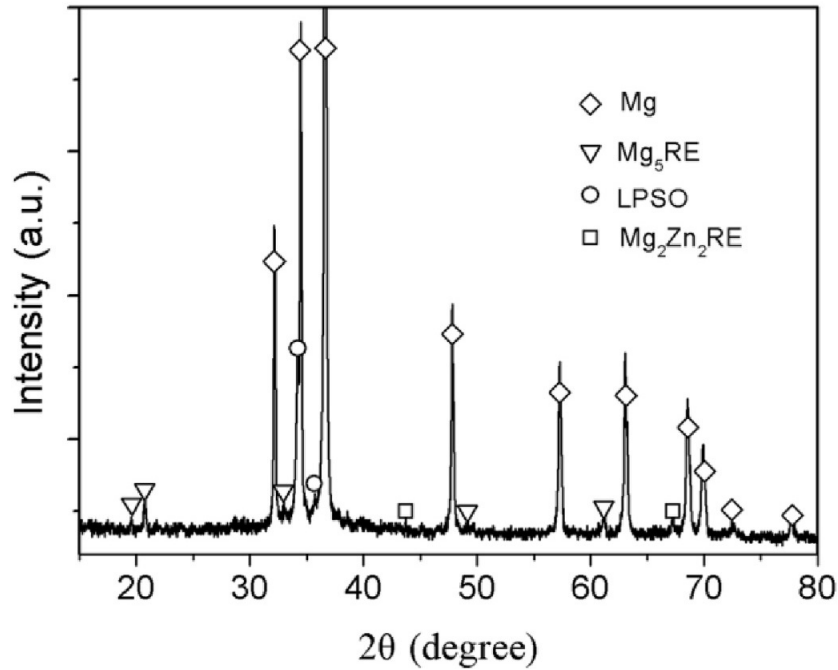


Figure 2: XRD pattern of the as-cast GYZK8310 alloy.

which are ordinarily distributed at grain boundaries and near grain boundaries, respectively, were defined as the lamellae phase and the plate-like phase, respectively. In addition, there are a number of round-shaped intermetallic particles located at grain boundaries or in α -Mg grains, with sizes of approximately 60e400 nm. These typed particles were frequently observed in Mg-RE-Zn-Zr systems and have been reported to be Zr-rich particles or Zn-Zr compounds [25-27]. Fig. 2 presents the XRD pattern of the as-cast GYZK8310 alloy. The results suggest that the dominant intermetallic phases are Mg_5RE (face-centered cubic structure, $a = 2.234$ nm [28]), Mg_2Zn_2RE which was always denoted as W phase (face-centered cubic structure, $a = 0.683$ nm [28]) and the LPSO phase. In the following, the crystal structures of the intermetallic phases will be analyzed using TEM.

Fig. 3a manifests the representative brightfield TEM (BF-TEM) image of the lamellae phase. It often has very large sizes, with the width over 1 μ m. According to the corresponding selected area electron diffraction (SAED) patterns (Fig. 3b and c), and the point EDS spectrum (Fig. 3d), the lamellae phase was identified as Mg_5RE and contains quite a few of Zn. This result is different with that the dominant intermetallic phase in the Mg-8Gd-1.2Zn-0.5Zr alloy is Mg_3Gd (face-centered cubic structure, $a = 0.7356$ nm) [12]. However, it is highly consistent with that reported for the Mg-Gd-Y-based alloys [14,16]. Furthermore, not all of

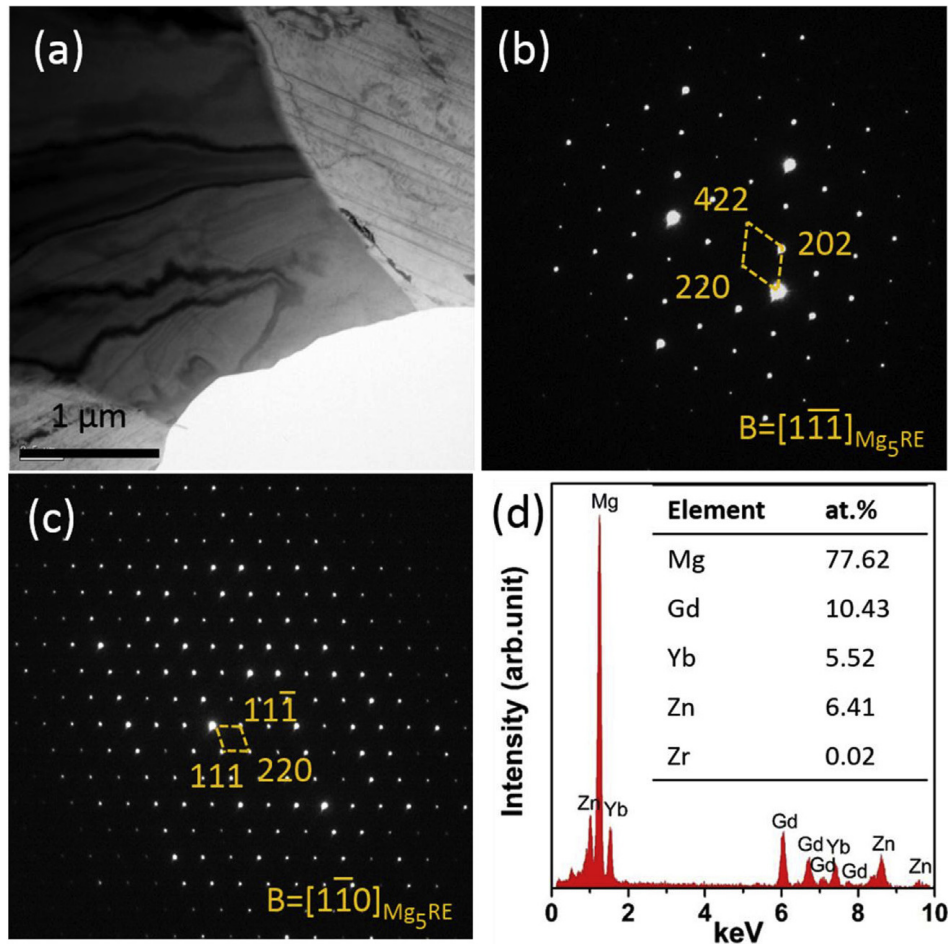


Figure 3: (a) BF-TEM image, (b and c) the corresponding SAED patterns and (d) the point EDX spectrum along with the analysis results of the lamellae phase in the as-cast GYZK8310 alloy.

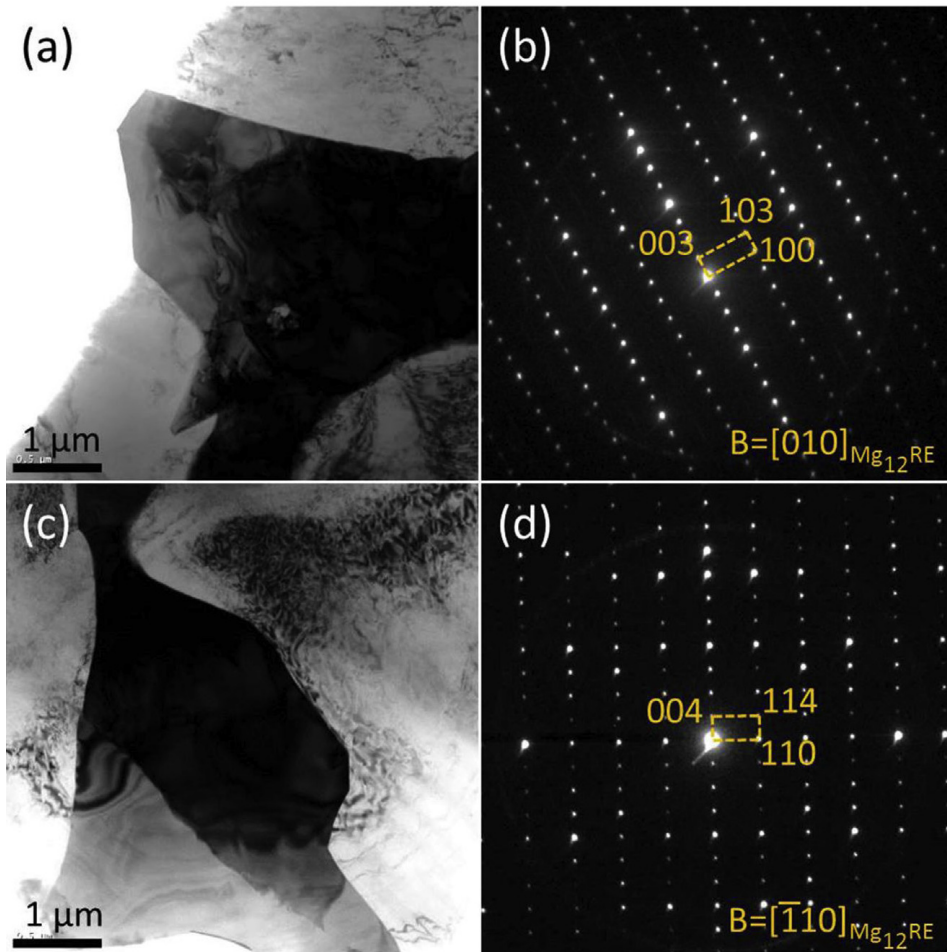


Figure 4: (a, c) BF-TEM images and (b, d) the corresponding SAED patterns of the lamellae intermetallic particles which are not Mg_5RE in the as-cast GYZK8310 alloy.

the lamellae intermetallic phases in the studied alloy are the Mg_5RE phase. According to amounts of TEM characterizations, the volume fraction of the lamellae particles which are not Mg_5RE , such as representatively shown in Fig. 4a and c, is approximately 8%. This phase is ordinarily composed of several parts. The corresponding SAED patterns from individual part (Fig. 4b and d) illustrate that the lamellae phase is an ordered $Mg_{12}RE$ phase (body-centered tetragonal structure, $a = 1.033$ nm and $c = 7.75$ nm [29]). Generally, $Mg_{12}RE$ phase was reported in Mg-Ce/La systems and has a tetragonal structure with lattice parameters of $a = 1.033$ nm and $c = 0.5964$ nm [30,31]. Only above the eutectic, an ordered $Mg_{12}RE$ structure can be observed [29,32]. Subsequently, the lamellae $Mg_{12}RE$ phase in the studied alloy might form during solidification when the temperature is above the eutectic. In addition, there is no identical orientation relationship (OR) between any two adjacent $Mg_{12}RE$ parts, or between Mg_5RE and $Mg_{12}RE$. Therefore, the $Mg_{12}RE$ phase would homogeneously form in the melt and the previously formed $Mg_{12}RE$ particles would not act as nucleation sites for the Mg_5RE phase.

Fig. 5a presents the high-angle annular darkfield scanning TEM (HAADF-STEM) image of the blocky phase that is labeled as B in Fig. 1b. This phase seems to be formed by amounts of the brighter rod-like particles being embedded in a relatively darker particle. Thus, the blocky particle probably contains two intermetallic phases: one is defined as the rod-like phase and the other one is defined as the blocky matrix phase. According to Fig. 5b, the rod-like phase has width of 10-300 nm and length of 0.05-3 μ m. The corresponding SAED pattern suggests that the blocky particle simultaneously contains both $Mg_{12}RE$ and W. Fig. 5c shows the high-resolution TEM (HR-TEM) image of a small short rod-like phase. The corresponding FFT patterns from the rod-like phase (highlighted by an orange dotted box) and the blocky matrix phase (highlighted by a red dotted box) were shown in Fig. 5e and f, respectively. The results indicate that the rod-like phase is W and the blocky matrix phase is the ordered $Mg_{12}RE$ phase. Furthermore, the W phase is coherent with the blocky matrix $Mg_{12}RE$ phase, following a crystallographic OR as $[0\bar{1}1]_w//[2\bar{3}0]Mg_{12}RE$, and $(\bar{1}11)_w//(001)Mg_{12}RE$. Fig. 5g shows the magnified HAADF-STEM image along with the corresponding EDS mappings of Mg, Gd, Yb and Zn elements for the region highlighted by a green dotted box. The results indicate that Yb is clearly enriched in the blocky matrix $Mg_{12}RE$ phase while both Gd and Zn in the rod-like W phase. Fig. 6a shows another irregular intermetallic phase. The EDS mappings of Mg, Gd, Yb and Zn elements for the region highlighted by a blue dotted box were shown in Fig. 6b. The results directly manifest four different regions which were labeled as A to D. A region contains Gd and Zn, but almost no Yb. B region has clearly weaker brightness than the other three regions and contains relatively less Gd and Zn than A region, but it also contains Yb. C region is similar to A region, but

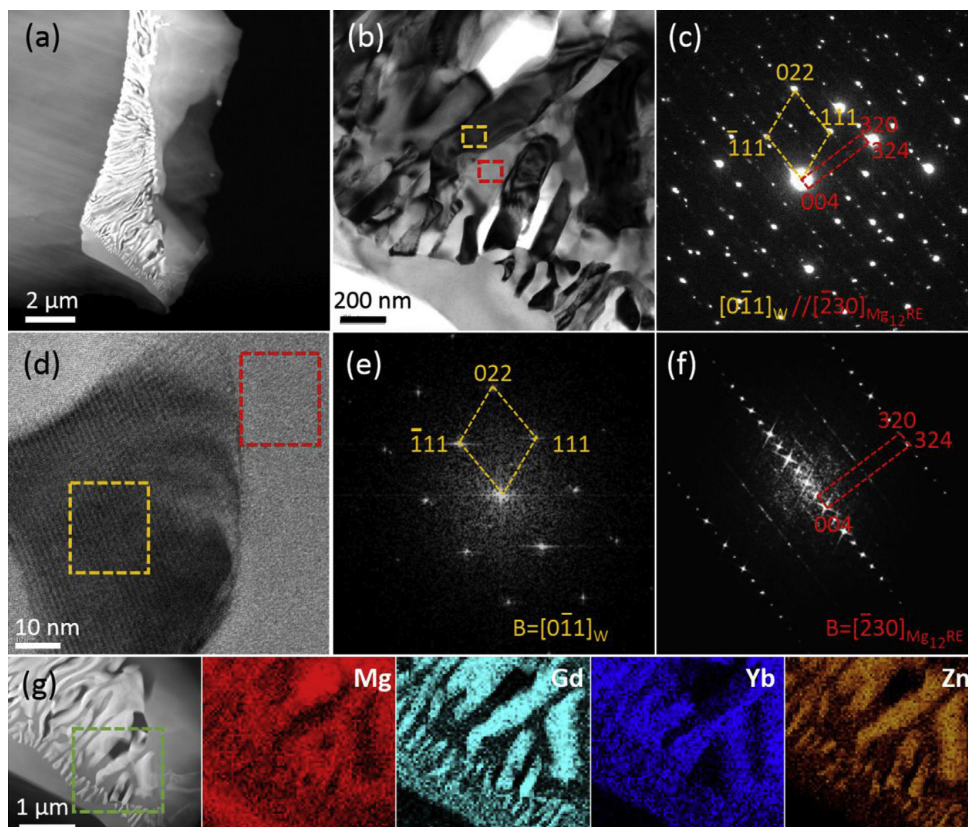


Figure 5: (a) HAADF-STEM image, (b) BF-TEM image and (c) the corresponding SAED pattern of the blocky particle that is labeled as B in Fig. 1b, (d) the corresponding HR-TEM image along with (e, f) the FFT patterns from local regions indicated by orange and red dotted boxes, respectively, and (g) the magnified HAADF-STEM image along with the EDS mappings of Mg, Gd, Yb and Zn elements for the region indicated by a green dotted box. (For interpretation of the references to colour in this figure legend, the reader is referred to the Web version of this article.)

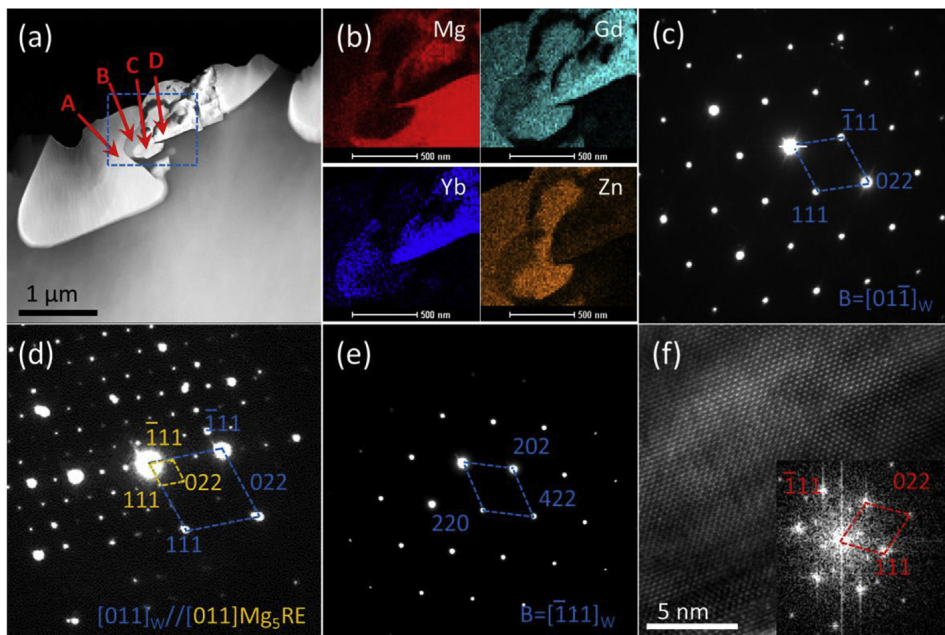


Figure 6: (a) HAADF-STEM image of an irregular blocky intermetallic phase, (b) the EDS mappings of Mg, Gd, Yb and Zn elements for the region highlighted by a blue dotted box in figure (a), (c-e) the corresponding SAED patterns and (f) the HR-TEM image along with the FFT pattern. (For interpretation of the references to colour in this figure legend, the reader is referred to the Web version of this article.)

it contains clearly more Zn than A region. D region contains relatively more Gd and Yb than the other regions although its Zn content is obviously lower than the other regions. Therefore, these four regions possibly correspond to four different intermetallic phases. According to the corresponding SAED patterns (Fig. 6c-e), the A-C phases were identified as W, Mg₅RE, and W, respectively. Furthermore, the Mg₅RE phase is coherent with the W phase, following an OR as $[0\bar{1}1]_w//[011]_{\text{Mg}_5\text{RE}}$, and $(111)_W//(111)_{\text{Mg}_5\text{RE}}$. Fig. 6g demonstrates the HR-TEM image along with the FFT pattern of the D phase. The result demonstrates that this phase is Mg_{0.0405}RE_{0.9595} (face-centered cubic structure, $a = 5.426$ nm [33]). This phase was infrequently observed in the studied alloy and always coexists with other intermetallic phases. Furthermore, this phase has not been reported in the previous open literature.

As indicated in Fig.1b, there are also amounts of fine LPSO plates that ordinarily distributes near grain boundaries. Fig. 7a gives the representative BF-TEM image of the microstructure near a grain boundary. The result illustrates that the LPSO plates parallelly distributed in the α -Mg matrix. The magnified BF-TEM and HAADF-STEM images were shown in Fig. 7b and c, respectively. The length and width of the LPSO plates are over 5 nm and approximately 2 nm, respectively. According to the corresponding HR-TEM image (Fig. 7d), these plates were deduced to belong to 14H typed LPSO phase (an ordered hexagonal structure, $a = 1.112$ nm, $c = 3.647$ nm [34]). This result is well in line with that reported in the previously work [12]. Additionally, there are also a few of coarse LPSO plates, such as shown in Fig. 8a. Their width is generally over 0.3 μm . According to the corresponding SAED pattern (Fig. 8b), the coarse LPSO phase owns the same structures as the fine LPSO plate.

3.2 Microstructure of the as-extruded GYZK8310 alloy

Fig. 9a shows the backscatter SEM image of the as-extruded GYZK8310 sample. The microstructure belongs to the obvious bimodal-grained structure consisted of coarse elongated un-recrystallized grains and fine dynamically recrystallized (DRXed) grains. This as-extruded microstructure was frequently observed in Mg-based alloys [10,35]. Additionally, extrusion stringers composed of numerous disintegrated intermetallic particles can be clearly observed. However, most extrusion stringers are tortuous and approximately parallel to the ED. Furthermore, there are also amounts of relatively fine intermetallic particles in the regions near the extrusion stringers or at the boundaries of the un-recrystallized grains (Fig. 9b).

In this work, an EBSD analysis was also performed on the as-extruded sample. Fig. 10a shows the inverse pole figure (IPF) map with ED being horizontal. Clear DRXed and un-recrystallized regions can be observed. The DRXed regions

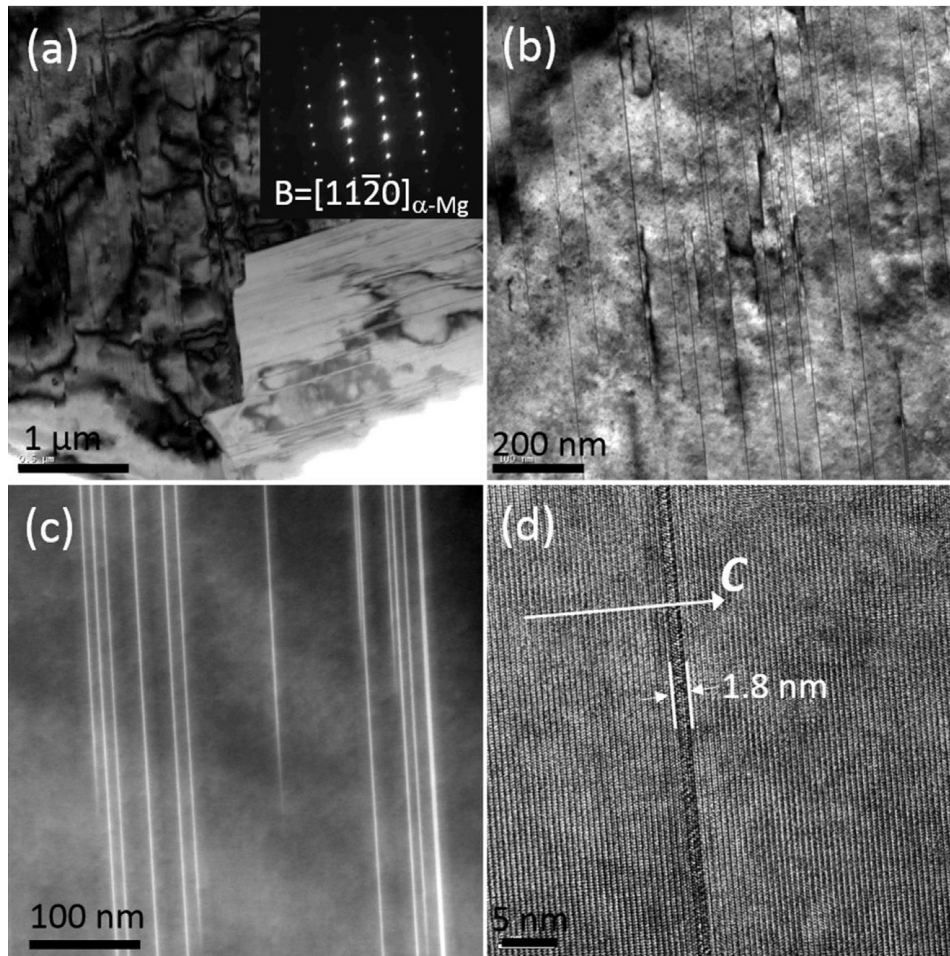


Figure 7: (a) BF-TEM image, the magnified (b) BF-TEM image and (c) HAADF-STEM image, and (d) the HR-TEM image of the fine LPSO plates near the grain boundaries.

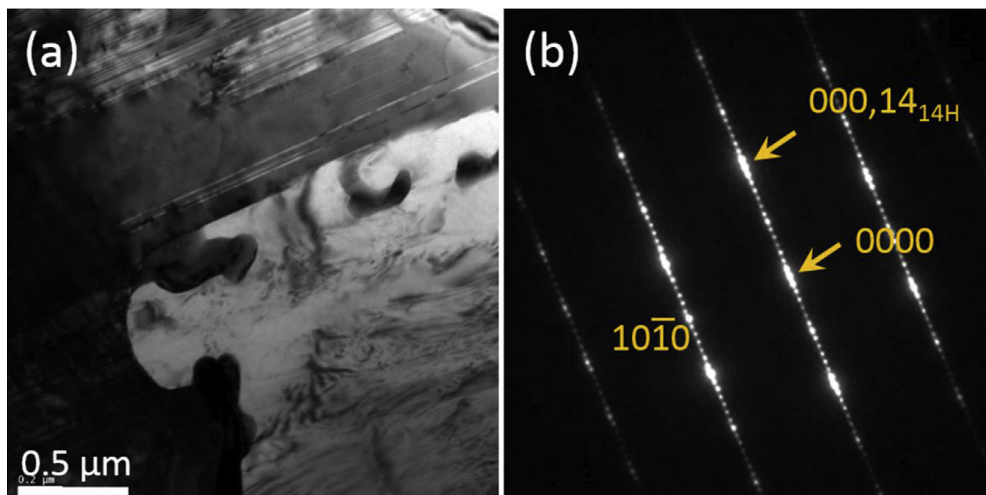


Figure 8: (a) BF-TEM image and (b) the corresponding SAED pattern of the coarse LPSO plate.

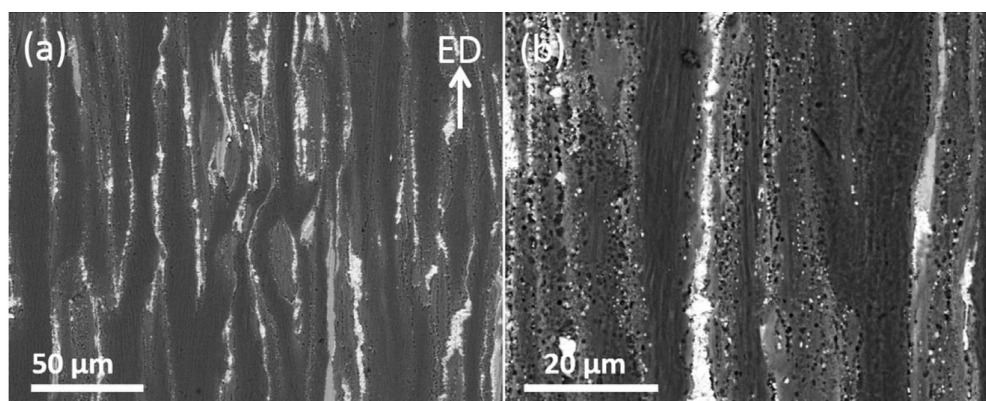


Figure 9: Backscatter SEM micrographs of the as-extruded GYZK8310 alloy.

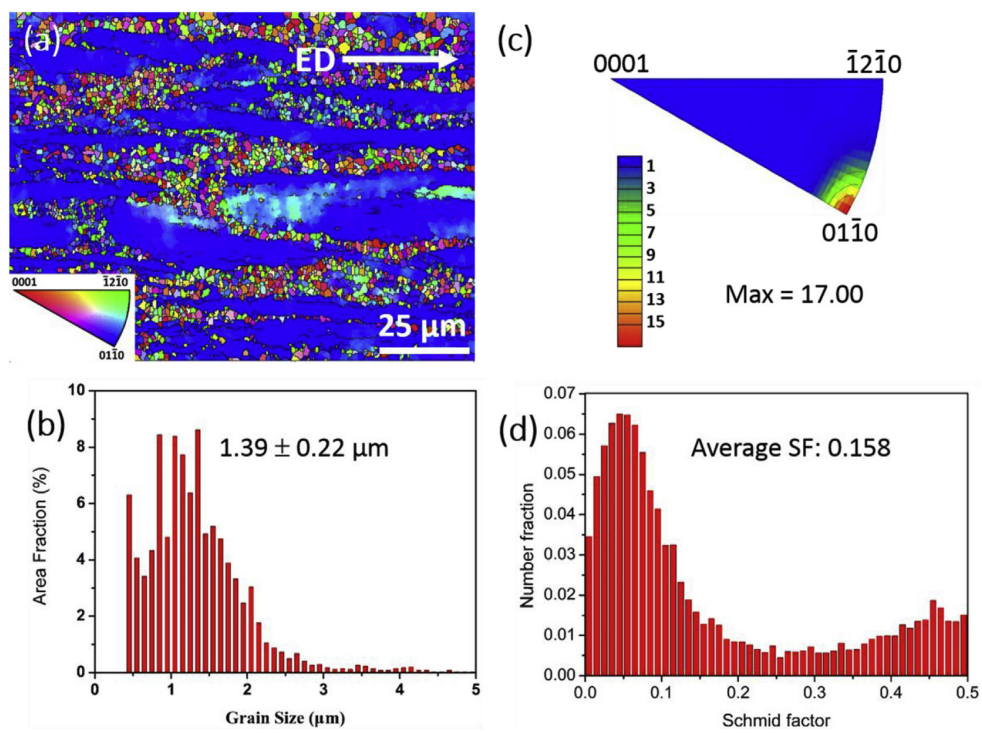


Figure 10: (a) Typical inverse pole figure (IPF) map, (b) grain size distribution histogram, (c) the corresponding IPF, and (d) the calculated (0001) $\langle 1120 \rangle$ Schmid factor (SF) distribution along ED.

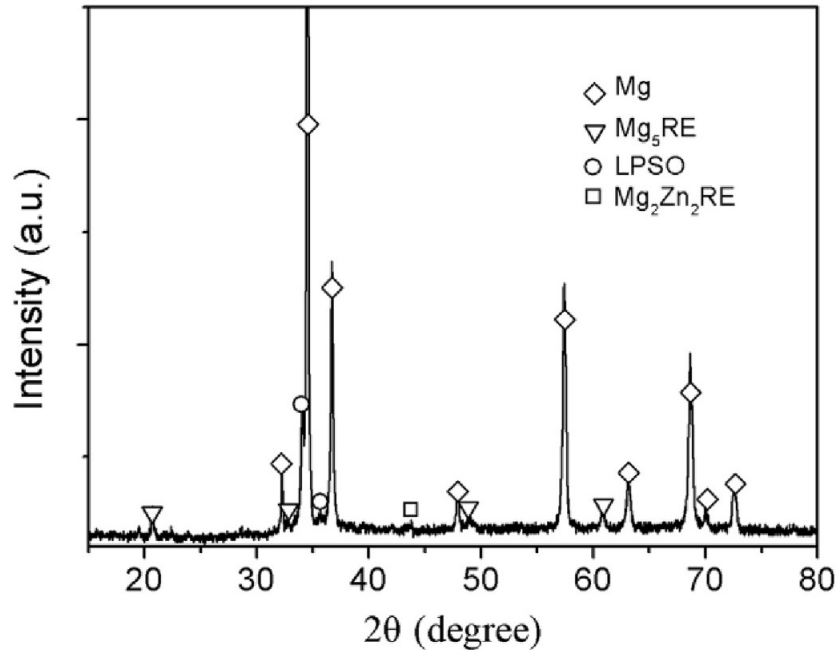


Figure 11: XRD pattern of the as-extruded GYZK8310 alloy.

present zonal along ED and mainly distribute at the un-recrystallized grain border. Furthermore, the DRXed regions contain numerous equiaxial grains. According to the histogram (Fig. 10c), the average sizes of the DRXed grains is 1.39 ± 0.22 μm . In addition, the corresponding statistical analysis reveals that the volume fraction of the un-recrystallized regions in the as-extruded sample is very high to approximately 81%. Fig. 10c illustrates the corresponding IPF in the form of a contour plot. The texture in the as-extruded GYZK8310 sample belongs to the typical $\langle 1010 \rangle$ fiber texture of the extruded Mg alloys [36,37]. It is well reported that adding RE elements into magnesium alloys can weaken the tendency of magnesium to retain a sharp texture during recrystallization [38]. Therefore, the so-called RE texture was frequently observed in many Mg-RE-based alloys [39,40]. However, no discernible "RE texture" orientation (i.e. $\langle 1121 \rangle // \text{ED}$) was observed in this work. Additionally, the maximum intensity of the texture in the as-extruded GYZK8310 alloy is approximately 17, which is comparative with the Mg-8.2Gd-3.8Y-1.0Zn-0.4Zr alloy [13]. Fig. 10d presents the calculated (0001) $\langle 1120 \rangle$ Schmid factor distribution along ED. The result indicates that the main deformation mechanism is basal slip [41]. Therefore, the as-extruded GYZK8310 alloy would exhibit excellent room temperature strengthening.

As indicated in Fig. 9, there are amounts of intermetallic phases in the as-extruded GYZK8310 alloy. Fig.11 shows the corresponding XRD pattern. The

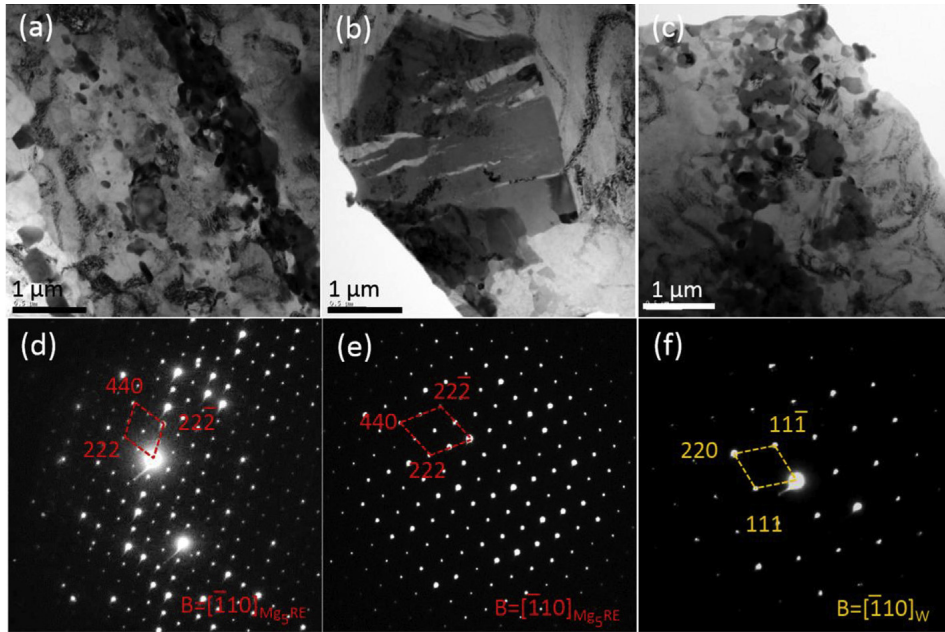


Figure 12: (aec) BF-TEM micrographs and (def) the corresponding SAED patterns of the disintegrated intermetallic phases at extrusion stringers.

result indicates that the dominant intermetallic phases are unaltered after extrusion. To well examine the structure of the dominant intermetallic phases and the new fine precipitates formed during extrusion, TEM characterizations were conducted. Fig. 12aec present the representative BF-TEM images of the disintegrated intermetallic particles at the extrusion stringers. According to the corresponding SAED patterns (Fig. 12def), most of the disintegrated blocky phases particularly the large cracked ones (with diameter over 2 mm) are Mg_5RE while a part of them are W. Fig. 13a shows the BF-TEM image of another kind of intermetallic particle at extrusion stringers. This particle seems to be combined with many small blocky particles being embedded in another matrix phase. Based on the corresponding SAED patterns (Fig. 13b and c), the embedded small phase is W while the matrix phase is the ordered $Mg_{12}RE$ phase. Additionally, the W phase is still coherent with the $Mg_{12}RE$ phase, following the same OR as that in the as-cast sample. Therefore, the OR between W and $Mg_{12}RE$ remains unaltered during extrusion. Fig. 13d illustrates the HAADF-STEM image of the combined particle. It is obvious that the W phase mainly distributes on the sides of the $Mg_{12}RE$ phase. Unlike that the W phase approximately orderly distributed in the $Mg_{12}RE$ phase in the as-cast sample, the W phase seems to be disturbed after extrusion. According to the corresponding EDS mappings of Mg, Gd, Yb, and Zn elements

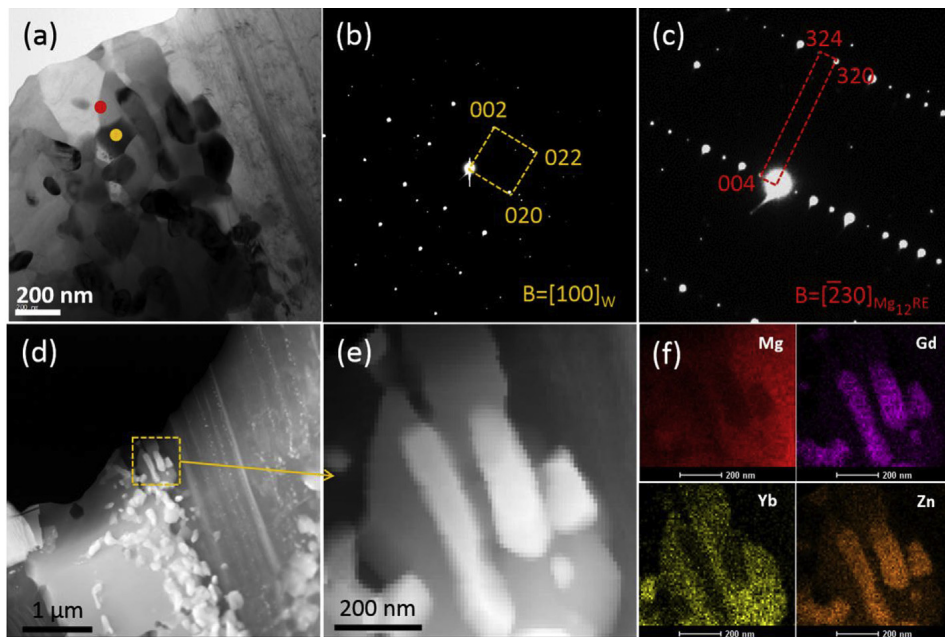


Figure 13: (a) BF-TEM micrograph of the disintegrated particle composed of two kinds of intermetallic phases, (b, c) the corresponding SAED patterns from the orange and red points, respectively, (d) the corresponding HAADF-STEM image, (e) the magnified HAADF-STEM image of the region indicated by an orange dotted box in figure (d), and (f) the corresponding EDS mappings of Mg, Gd, Yb and Zn elements. (For interpretation of the references to colour in this figure legend, the reader is referred to the Web version of this article.)

(Fig. 13f) for the region highlighted by an orange dotted box in Fig.13d (the magnified image is shown in Fig.13e), Gd and Zn are obviously enriched in the W phase while Yb is enriched in the $Mg_{12}RE$ phase. This is fully consistent with that for the combined particle in the as-cast sample.

As revealed in the as-cast microstructural analysis, some particles are composed of W and Mg_5RE . In the as-extruded sample, such particle was also observed such as shown in Fig. 14a. It ordinarily discretely distributes in the DRXed region. Fig. 14b and c manifest the corresponding SAED patterns and the HR-TEM image along with FFT patterns. The results indicate that the relatively small part belongs to W while the relatively large part belongs to Mg_5RE . They are still coherent and follow the same OR as that revealed in the as-cast sample.

Fig. 15a and b show the representative BF-TEM images of dynamically precipitated intermetallic phases in the DXRed region. They generally present blocky and distributed at DRXed grain boundaries. In addition, their diameter is approximately 180 nm. From the corresponding SAED patterns (Fig. 15c and d), these dynamically precipitated intermetallic phases were identified as Mg_5RE . Fig. 15e manifests the HAADF-STEM image along with the corresponding EDS mappings of Mg, Gd, Yb and Zn elements for a typical precipitate. The results suggest that the dynamically precipitated Mg_5RE phase mainly contains Gd, Yb and Zn, which is well in line with that for the Mg_5RE phase formed during solidification. In addition, amounts of fine parallel plates were also observed in the as-extruded GYZK8310 alloy (Fig. 16a). The plates near grain boundaries always own relatively greater width (approximately 40 nm) while those in grain center have relatively smaller width (approximately 18 nm). The corresponding SAED pattern (Fig. 16b) and HR-TEM image along with FFT pattern (Fig. 16c) demonstrate that these parallel plates are the 14H-type LPSO phase. Generally, the parallel 14H-LPSO plates distribute in the region near the extrusion stringers (Fig. 16d). The LPSO phases can improve the resistance to deformation of Mg during hot-extrusion, resulted in relatively small strain energy accumulation. This results in no enough driving force for recrystallization in the LPSO-containing Mg matrix. Thus, the LPSO plates would inhibit recrystallization during hot-extrusion. In addition, kink bands are formed in the LPSO plates (Fig. 16e). LPSO plates can effectively impede dislocation motion. Amounts of dislocation lines will interact with the LPSO plates during deformation, which results in obvious dislocation accumulation in the LPSO-containing region. This further confirms that the LPSO plates can improve resistance to deformation. Therefore, the large volume fraction of un-recrystallized regions in the as-extruded GYZK8310 alloy is possibly related to amounts of LPSO plates in Mg matrix. Moreover, LPSO plates were also observed in a few of DRXed grains (Fig. 16f). Thus, extra LPSO plates could form during hot-extrusion.

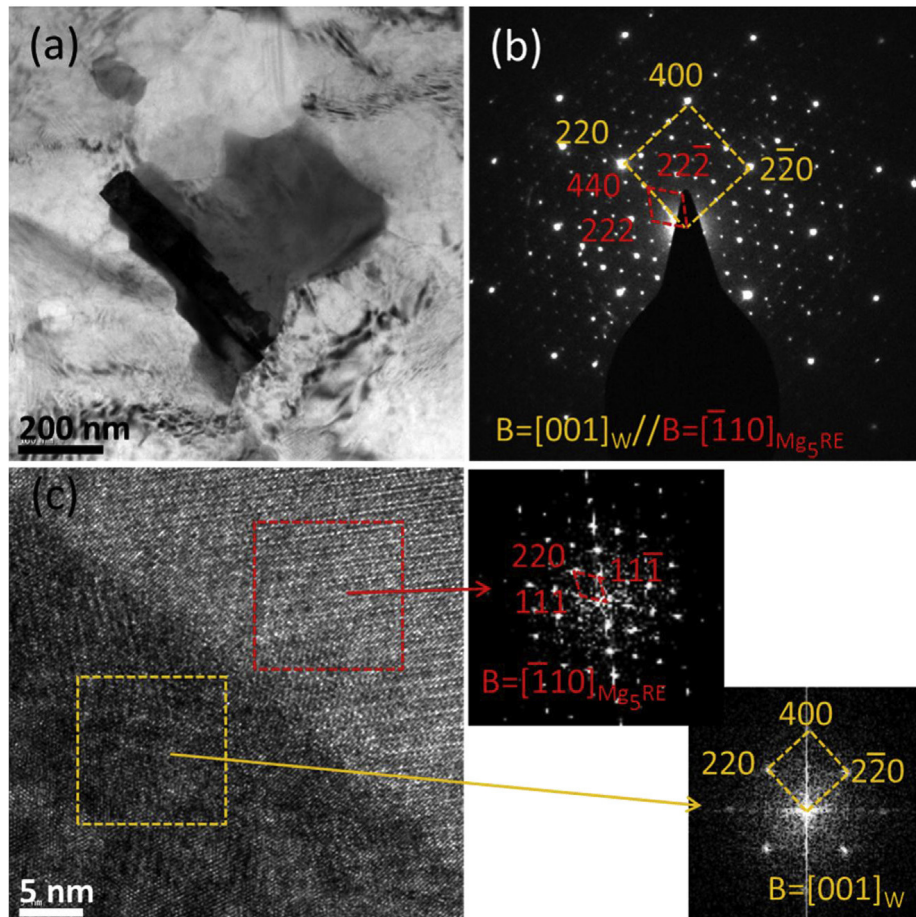


Figure 14: (a) BF-TEM image and (b) the corresponding SAED pattern of a blocky intermetallic particle consisted of two intermetallic phases, (c) the corresponding HR-TEM image along with the FFT patterns from local regions indicated by orange and red dotted boxes. (For interpretation of the references to colour in this figure legend, the reader is referred to the Web version of this article.)

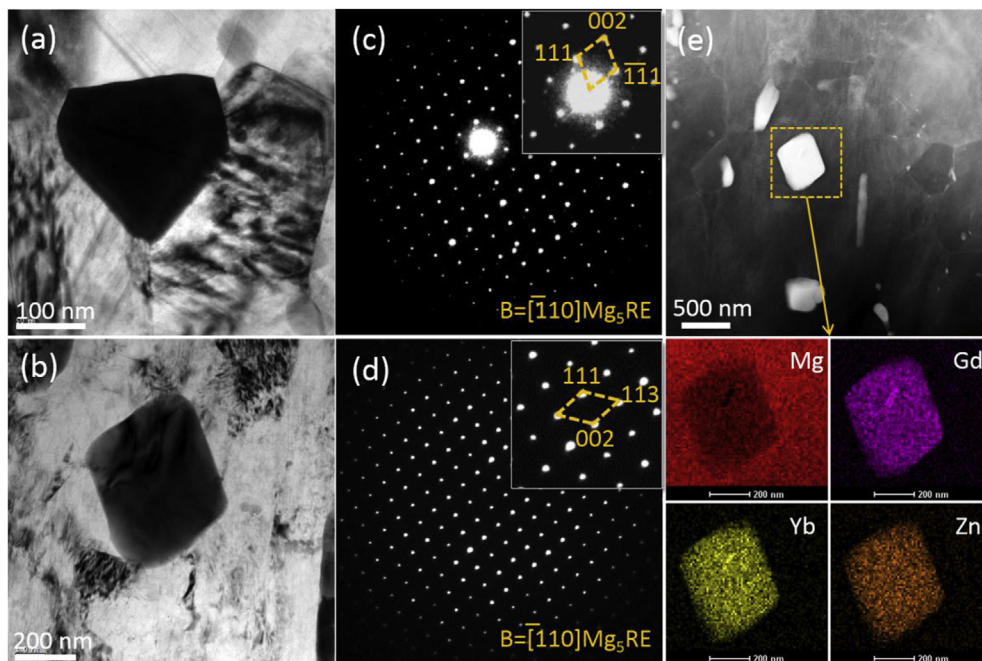


Figure 15: (a, b) BF-TEM images along with (c, d) the corresponding SAED patterns for the dynamically precipitated particles, and (e) the corresponding HAADF-STEM image along with the EDS mappings of Mg, Gd, Yb, and Zn elements for a typical Mg_5RE precipitate.

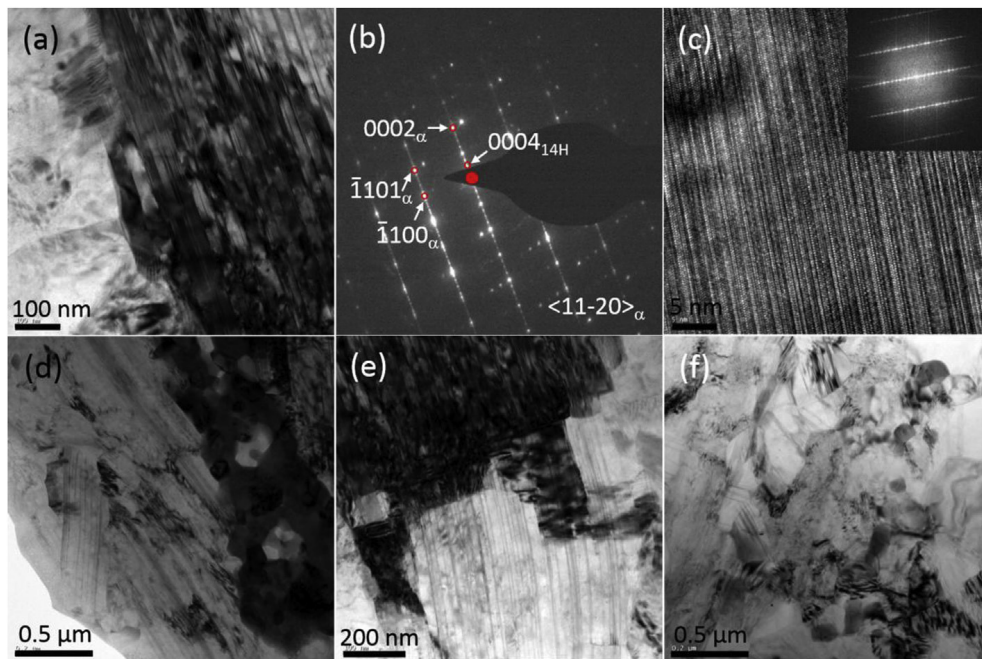


Figure 16: (a) BF-TEM image, (b) the corresponding SAED pattern and (c) the corresponding HR-TEM image along with the FFT pattern of the LPSO plates in the un-recrystallized regions, and (def) BF-TEM images of LPSO plates in (d, e) the un-recrystallized regions and (f) the DRXed grains.

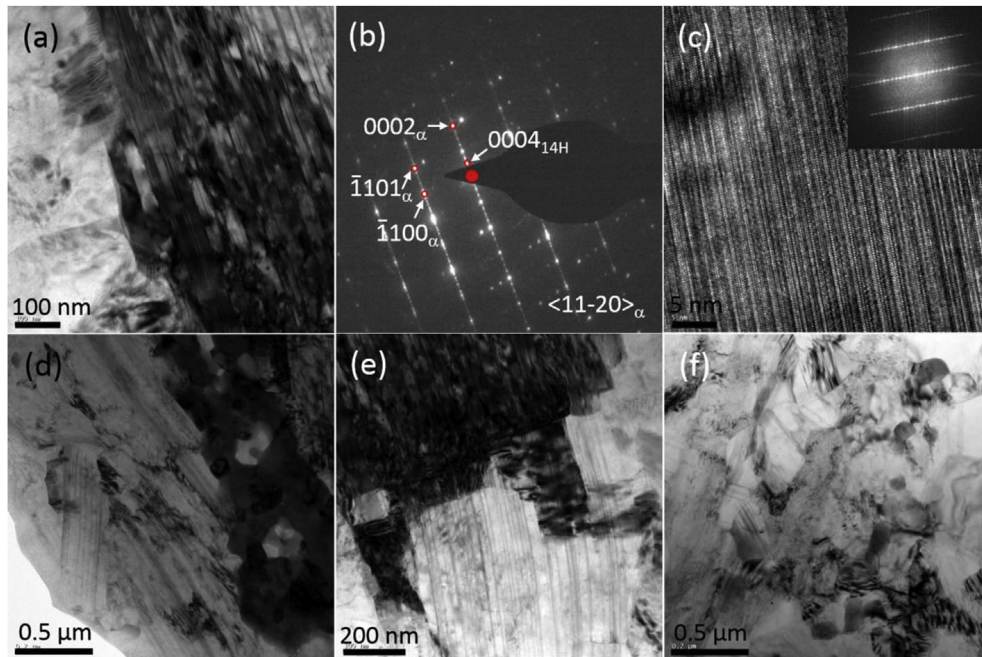


Figure 17: Representative tensile engineering stress-strain curves of the as-extruded GYZK8310 alloy at both RT and high temperatures.

3.3 Mechanical properties of the GYZK8310 alloy

Fig. 17 presents the representative engineering tensile stress-strain curves of the as-extruded GYZK8310 alloy at both RT and high temperatures. The results manifest that the as-extruded GYZK8310 alloy exhibits high YS although with relatively unremarkable strain hardening behavior even at RT. In addition, the alloy's strength decreases slowly as the testing temperature increases when the temperature is not over 250 °C. Moreover, the elongation of the GYZK8310 alloy increases as the testing temperature increases. To intuitively compare the strength of the as-extruded GYZK8310 alloy with quite a few of the classic Mg-Gd-based alloys which are with comparative or even higher RE additions, the tensile properties including UTS, YS, and elongation (?) are listed in Table 1. The as-extruded GYZK8310 alloy exhibits significantly higher strength than the alloys with similar compositions. For instance, at RT, the UTS and YS of the as-extruded GYZK8310 alloy are higher by approximately 30% and 81%, respectively, than the as-extruded Mg-8.2Gd-3.8Y-1.0Zn-0.4Zr alloy [13], and by approximately 21% and 58%, respectively, than the as-extruded Mg-9Gd-3Y-1.5Zn-0.5Zr alloy [42]. Further-more, the studied alloy even has higher strength than the traditional high-strength alloy with higher RE content. As an example, the UTS and

Table 1: Tensile properties including UTS (MPa), YS (MPa), and ϵ (%) of the as-extruded GYZK8310 alloy and the as-extruded conventional Mg-Gd(-Y)-Zn-Zr-based alloys with similar compositions.

Alloys (wt.%)	Temperature (°C)	UTS	YS	$V\epsilon$	Refs.
Mg-8.2Gd-3.8Y-1.0Zn-0.4Zr	RT	323	228	8.6	[13]
Mg-9Gd-3Y-1.5Zn-0.5Zr	RT	350	261	10.5	[42]
Mg-8Gd-1Zn-0.4Zr	RT	25	285	200	[53]
Mg-11Gd-4.5Y-1Nd-1.5Zn-0.5Zr	RT	377	327	3.8	[16]
	200	357	290	5	
	250	286	268	10.5	
	300	193	172	54.4	
Mg-8Gd-2Y-1Nd-0.3Zn-0.6Zr	RT	271	143	18.7	[43]
	200	233	134	20.1	
	300	188	121	44	
Mg-8Gd-3Yb-1.2Zn-0.5Zr	RT	425	413	5.5	This
	200	400	370	7.1	work
	250	334	314	13	
	300	204	191	25.5	

YS of the studied alloy are higher by approximately 13% and 26%, respectively, than the as-extruded Mg-11Gd-4.5Y-1Nd-1.5Zn-0.5Zr alloy [16]. Moreover, the studied alloy owns better ductility. Finally, the as-extruded GYZK8310 alloy has excellent high-temperature strength. For example, the UTS and YS of the studied alloy are higher by approximately 72% and 176%, respectively, at 200 °C, and by approximately 9% and 58%, respectively, at 300 °C, than those of the as-extruded Mg-8Gd-2Y-1Nd-0.3Zn-0.6Zr alloy [43]. Additionally, the as-extruded GYZK8310 alloy has higher UTS and YS by approximately 12% and 28%, respectively, at 200 °C, by approximately 17% and 17%, respectively, at 250 °C, and by approximately 6% and 11%, respectively, at 300 °C than the as-extruded Mg-11Gd-4.5Y-1Nd-1.5Zn-0.5Zr alloy [16]. With respect to the extruded alloys, the superior YS (σ_y) was reported to be attributed to grain boundary strengthening ($\Delta\sigma_{gs}$), solid-solution strengthening ($\Delta\sigma_{ss}$), dislocation strengthening ($\Delta\sigma_{ds}$) and precipitation/dispersion strengthening ($\Delta\sigma_{ps}$). Thus, the YS of the as-extruded alloy can be estimated by the following equation [44,45]:

$$\sigma_y = \sigma_0 + \Delta\sigma_{gs} + \Delta\sigma_{ss} + \Delta\sigma_{ds} + \Delta\sigma_{ps} \quad (1)$$

where σ_0 is the intrinsic lattice resistance to basal slip for Mg ($\sigma_0 = 11$ MPa). For the as-extruded GYZK8310 alloy, the microstructure consists of DRXed and un-recrystallized grains. Thus, $\Delta\sigma_{gs}$ has to be calculated by the following equation [46]:

$$\Delta\sigma_{gs} = f_{un}\sigma_{un} + f_R\sigma_R \quad (2)$$

where f_{un} and f_R are the fractions of the un-recrystallized grains and DRXed grains, respectively, σ_{un} and σ_R are the yield strength of un-recrystallized grains (affected mainly by the Schmid factor) and DRXed grains, respectively. Both σ_{un} and σ_R can be calculated by the well-defined Hall-Petch relationship that can be found elsewhere [47]. Finally, $\Delta\sigma_{ds}$ was calculated to be approximately 58 MPa. It is well reported that the dislocation density (ρ) of the extruded Mg alloys is ordinarily estimated to be approximately $1.0 \cdot 10^{14} \text{ m}^{-2}$ [48]. Thus, the contribution to YS of dislocation strengthening can be estimated by Ref. [49]:

$$\Delta\sigma_{ds} = \alpha M G b \sqrt{\rho} \quad (3)$$

where α is a constant (0.2 [49]), M is Taylor factor taking value of the inverse of the measured Schmid factor, G is the shear modulus of Mg ($G = 17.2$ MPa [50]), and b is the Burgers vector ($b = 0.32$ nm [50]). In this work, the value of M is calculated to be 6.3. Thus, $\Delta\sigma_{ds}$ is approximately 69 MPa. Thirdly, there are still some dissolved Gd and Yb atoms in Mg matrix due to their subsistent solid solubility in Mg even at RT. According to Mg-Gd and Mg-Yb phase diagrams, the

atomic fractions of solutes of Gd and Yb in the as-extruded GYZK8310 alloy were estimated to be 0.085 at.% and 0.006 at.%, respectively. Then, the contribution to YS from solid-solution strengthening was calculated by the following equation as [51]:

$$\Delta\sigma_{ss} = CX^{\frac{2}{3}} \quad (4)$$

where C is the alloy strengthening rate. The solid-solution strengthening ($\Delta\sigma_{ss}$) was estimated to be approximately 48 MPa. Finally, except the disintegrated intermetallic particles at extrusion stringers, there are amounts of dynamically precipitated particles in the DRXed regions and fine LPSO plates in the unrecrystallized regions. The dynamically precipitated intermetallic particles can be regarded to be approximately spherical. Then, their contribution to YS can be calculated using the classical Orowan strengthening equation as follow [52]:

$$\Delta\sigma_{p1} = \frac{MGB}{2\pi\sqrt{1-\nu}} \frac{1}{\lambda} \ln \frac{d_p}{r_0} \quad (5)$$

where n is Poisson ratio ($n = 0.35$ [50]), λ is the distance of the precipitates, r_0 is the core radius of the dislocation line, and d_p is the mean diameter of the precipitates. With respect to the lamellae LPSO plates, the contribution to YS can be estimated by the modified Orowan equation for the basal lamellae precipitates, as follow:

$$\Delta\sigma_{p2} = \frac{MGB}{2\pi\sqrt{1-\nu} \left(\frac{0.953}{\sqrt{f}} - 1 \right) d_t} \ln \frac{t_t}{b} \quad (6)$$

where d_t and t_t are the uniform diameter and thickness, respectively, of the LPSO plates, and f is the volume fraction. Subsequently, $\Delta\sigma_{ps}$ can be calculated using the following equation as [46]:

$$\Delta\sigma_{gs} = f_{un}\sigma_{p1} + f_R\Delta\sigma_{p2} \quad (7)$$

According to above equation, the contribution to YS from precipitation/dispersion strengthening was calculated to be approximately 227 MPa. Therefore, the calculated value of σ_y is approximately 402 MPa, which is reasonably agreeable with the experimental value (413 MPa). The underestimation may be attributed to ignoring the contribution of disintegrated intermetallic particles. According to the above analysis, the dominant strengthening mechanism in the as-extruded GYZK8310 alloy is precipitation/dispersion strengthening. Since the RE-containing intermetallic phases generally have relatively outstanding thermal stability, they can efficiently impede dislocation motion even at high temperatures. As a result, the as-extruded GYZK8310 alloy also exhibits excellent high-temperature strength.

4 Conclusions

Microstructures and mechanical properties of a GYZK8310 alloy were investigated. The following conclusions can be drawn:

- The dominant intermetallic phases in the as-cast GYZK8310 alloy are Mg₅RE phase, 14H-type LPSO phase, W phase and ordered Mg₁₂RE phase. Ordinarily, W coexists with Mg₅RE or Mg₁₂RE, following an OR as $[0\bar{1}1]_w//[011]_{Mg_5RE}$, $(111)W// (111)Mg_5RE$, or $[0\bar{1}1]_w//[2\bar{3}0]_{Mg_{12}RE}$, $(\bar{1}11)_w//(001)_{Mg_{12}RE}$.
- After extrusion, the microstructure of the GYZK8310 alloy consists of un-recrystallized regions along with a small part of (approximately 19% volume fraction) DRXed regions. The alloy exhibits the typical $\langle 1010 \rangle$ fiber texture.
- The coarse Mg₅RE, W and Mg₁₂RE particles were dis-integrated during extrusion and distribute at extrusion stringers while the fine LPSO plates mainly distribute in un-recrystallized regions. Also, amounts of nanoscale Mg₅RE particles were dynamically precipitated in the DXRed regions
- The as-extruded GYZK8310 alloy exhibits clearly higher strength at both RT and high temperatures than the traditional Mg-Gd-Y-Zn-Zr-based alloys with comparative or even higher RE contents. The dominant strengthening mechanism was revealed as precipitation/dispersion strengthening.

Acknowledgements

This work was supported by the National Natural Science Foundation of China under grants no. 21521092, 51701200, 11804030, and the Project for Science & Technology Development of Jilin Province under grants no. 20180520004JH, 2015DFH50210, 201602011004GX, 2016SYHZ0006, 20170414001GH, and 20180520160JH.

References

1. Q. Yang, K. Guan, B. Li, F. Meng, S. Lv, Z. Yu, X. Zhang, J. Zhang, J. Meng, Coexistence of 14H and 18R-type long-period stacking ordered (LPSO) phases following a novel orientation relationship in a cast Mg-Al-RE-Zn alloy, *J. Alloys Compd.* 766 (2018) 902-907.

2. A.A. Luo, Recent magnesium alloy development for elevated temperature applications, *Int. Mater. Rev.* 49 (2004) 13-30.
3. W.J. Joost, P.E. Krajewski, Towards magnesium alloys for high-volume automotive applications, *Scr. Mater.* 128 (2017) 107-112.
4. S.H. Lv, Y.W. Li, X.L. Lü, F.Z. Meng, Q. Yang, D.M. Han, Q. Duan, J. Meng, The types and structures of the intermetallic phases in a cast Mg-4Al-15Gd-4Y-1Zn alloy, *J. Alloys Compd.* 731 (2018) 612-619.
5. X. Xia, W. Sun, A.A. Luo, D.S. Stone, Precipitation evolution and hardening in Mg-Sm-Zn-Zr alloys, *Acta Mater.* 111 (2016) 335-347.
6. A.A. Luo, R.K. Mishra, A.K. Sachdev, High-ductility magnesium-zinc-cerium extrusion alloys, *Scr. Mater.* 64 (2011) 410-413.
7. X. Gao, J.F. Nie, Enhanced precipitation-hardening in Mg-Gd alloys containing Ag and Zn, *Scr. Mater.* 58 (2008) 619-622.
8. Q. Yang, X. Qiu, S.H. Lv, F.Z. Meng, K. Guan, B.S. Li, D.P. Zhang, Y.Q. Zhang, X.J. Liu, J. Meng, Deteriorated tensile creep resistance of a high-pressure die-cast Mg-4Al-4RE-0.3Mn alloy induced by substituting part RE with Ca, *Mater. Sci. Eng. A* 716 (2018) 120-128.
9. T. Homma, N. Kunito, S. Kamado, Fabrication of extraordinary high-strength magnesium alloy by hot extrusion, *Scr. Mater.* 61 (2009) 644-647.
10. K. Guan, Q. Yang, F.Q. Bu, X. Qiu, W. Sun, D.P. Zhang, T. Zheng, X.D. Niu, X.J. Liu, J. Meng, Microstructures and mechanical properties of a high-strength Mg-3.5Sm-0.6Zn-0.5Zr alloy, *Mater. Sci. Eng. A* 703 (2017) 97-107.
11. J.H. Li, J. Barrirero, G. Sha, H. Aboufadel, F. Mücklich, P. Schumacher, Precipitation hardening of an Mg-5Zn-2Gd-0.4Zr (wt.%) alloy, *Acta Mater.* 108 (2016) 207-218.
12. B.S. Li, K. Guan, Q. Yang, X.D. Niu, D.D. Zhang, Z.J. Yu, X.H. Zhang, Z.M. Tang, J. Meng, Effects of 0.5 wt.% Ce addition on microstructures and mechanical properties of a wrought Mg-8Gd-1.2Zn-0.5Zr alloy, *J. Alloys Compd.* 763 (2018) 120-133.
13. C. Xu, M.Y. Zheng, K. Wu, E.D. Wang, G.H. Fan, S.W. Xu, S. Kamado, X.D. Liu, G.J. Wang, X.Y. Lv, Influence of rolling temperature on the microstructure and mechanical properties of Mg-Gd-Y-Zn-Zr alloy sheets, *Mater. Sci. Eng. A* 559 (2013) 615-622.

14. X.B. Zheng, W.B. Du, Z.H. Wang, S.B. Li, K. Liu, X. Du, Remarkably enhanced mechanical properties of Mg-8Gd-1Er-0.5Zr alloy on the route of extrusion, rolling and aging, *Mater. Lett.* 212 (2018) 155-158.
15. W. Rong, Y. Zhang, Y.J. Wu, M. Sun, J. Chen, Y. Wang, J.Y. Han, L.M. Peng, H.X. Ding, Effects of Zr and Mn additions on formation of LPSO structure and dynamic recrystallization behavior of Mg-15Gd-1Zn alloy, *J. Alloys Compd.* 692 (2017) 805-816.
16. Z.J. Yu, Y.D. Huang, X. Qiu, Q. Yang, W. Sun, Z. Tian, D.P. Zhang, J. Meng, Fabrication of magnesium alloy with high strength and heat-resistance by hot extrusion and aging, *Mater. Sci. Eng. A* 578 (2013) 346-353.
17. A.V. Dobromyslov, L.I. Kaigorodova, V.D. Sukhanov, T.V. Dobatkina, Decomposition of a supersaturated solid solution in the Mg-3.3 wt.% Yb alloy, *Phys. Met. Metallogr.* 103 (2007) 64-71.
18. W.B. Yu, Z.Y. Liu, H. He, N.D. Cheng, X.L. Li, Microstructure and mechanical properties of ZK60eYb magnesium alloys, *Mater. Sci. Eng. A* 478 (2008) 101-107.
19. D. Zhang, D. Zhang, F. Bu, X. Li, B. Li, T. Yan, K. Guan, Q. Yang, X.J. Liu, J. Meng, Excellent ductility and strong work hardening effect of as-cast Mg-Zn-Zr-Yb alloy at room temperature, *J. Alloys Compd.* 728 (2017) 404-412.
20. S.M. Jo, K.C. Park, B.H. Kim, H. Kimura, S.K. Park, Y.H. Park, Investigation on the microstructure and mechanical properties of Mg-Al-Yb alloys, *Mater. Trans.* 52 (2011) 1088-1095.
21. J.F. Nie, X. Gao, S.M. Zhu, Enhanced age hardening response and creep resistance of Mg-Gd alloys containing Zn, *Scr. Mater.* 53 (2005) 1049-1053.
22. T. Honma, T. Ohkubo, S. Kamado, K. Hono, Effect of Zn additions on the age hardening of Mg-2.0Gd-1.2Y-0.2Zr alloys, *Acta Mater.* 55 (2007) 4137-4150.
23. G. Li, J. Zhang, R. Wu, Y. Feng, S. Liu, X. Wang, Y. Jiao, Q. Yang, J. Meng, Development of high mechanical properties and moderate thermal conductivity cast Mg alloy with multiple RE via heat treatment, *J. Mater. Sci. Technol.* 34 (2018) 107-1084.
24. K. Guan, B.S. Li, Q. Yang, D.D. Zhang, X.H. Zhang, J.Q. Zhang, L. Zhao, X.J. Liu, J. Meng, Microstructural characterization of intermetallic phases in a solution-treated Mg-5.0Sm-0.6Zn-0.5Zr (wt.%) alloy, *Mater. Char.* 145 (2018) 329-336.
25. X. Wu, F. Pan, R. Cheng, S. Luo, Effect of morphology of long period stacking ordered phase on mechanical properties of Mg-10Gd-1Zn-0.5Zr magnesium alloy, *Mater. Sci. Eng. A* 726 (2018) 64-68.

26. X.Z. Han, W.C. Xu, D.B. Shan, Effect of precipitates on microstructures and properties of forged Mg-10Gd-2Y-0.5Zn-0.3Zr alloy during ageing process, *J. Alloys Compd.* 509 (2011) 8625-8631.
27. Z. He, L. Peng, P. Fu, Y. Wang, X. Hu, W. Ding, High cycle fatigue improvement by heat-treatment for semi-continuous casting Mg96.34Gd2.5Zn1Zr0.16 alloy, *Mater. Sci. Eng. A* 604 (2014) 78-85.
28. J.F. Nie, Precipitation and hardening in magnesium alloys, *Metall. Mater. Trans. A* 43 (2012) 3891-3939.
29. D.H. Wood, E.M. Cramer, Phase relations in the magnesium-rich portion of the cerium-magnesium system, *J. Less Common. Met.* 9 (1965) 321e-37.
30. X. Zhang, D. Kevorkov, I. Jung, M. Pekguleryuz, Phase equilibria on the ternary Mg-Mn-Ce system at the Mg-rich corner, *J. Alloys Compd.* 482 (2009) 420-428.
31. M. Celikin, A.A. Kaya, R. Gauvin, M. Pekguleryuz, Effects of manganese on the microstructure and dynamic precipitation in creep-resistant cast Mg-Ce-Mn alloys, *Scr. Mater.* 66 (2012) 737-740.
32. Q.C. Johnson, G.S. Smith, D.H. Wood, E.M. Cramer, A new structure in the magnesium-rich region of the cerium-magnesium system, *Nature* 201 (1964), 600-600.
33. O.D. McMasters, K.A. Gschneidner jr., Ytterbium-magnesium system, *J. Less Common. Met.* 8 (1965) 289-298.
34. Y. Michiaki, A. Tsutomu, Y. Shintaro, K. Yoshihito, Mechanical properties of warm-extruded Mg-Zn-Gd alloy with coherent 14H long periodic stacking ordered structure precipitate, *Scr. Mater.* 53 (2005) 799-803.
35. K. Oh-ishi, C.L. Mendis, T. Homma, S. Kamado, T. Ohkubo, K. Hono, Bimodally grained microstructure development during hot extrusion of Mg-2.4Zn-0.1Ag-0.1Ca-0.16Zr (at.%) alloys, *Acta Mater.* 57 (2009) 5593-5604.
36. T. Al-Samman, X. Li, Sheet texture modification in magnesium-based alloys by selective rare earth alloying, *Mater. Sci. Eng. A* 528 (2011) 3809-3822.
37. I. Basu, T. Al-Samman, Triggering rare earth texture modification in magnesium alloys by addition of zinc and zirconium, *Acta Mater.* 67 (2014) 116-133.
38. N. Stanford, D. Atwell, M.R. Barnett, The effect of Gd on the recrystallisation, texture and deformation behaviour of magnesium-based alloys, *Acta Mater.* 58 (2010) 6773-6783.
39. R. Alizadeh, R. Mahmudi, A.H.W. Ngan, T.G. Langdon, An unusual extrusion texture in Mg-Gd-Y-Zr alloys, *Adv. Eng. Mater.* 18 (2016) 1044-1049.

40. Z.B. Chen, C.M. Liu, H.C. Xiao, J.K. Wang, Z.Y. Chen, S.N. Jiang, Z.J. Su, Effect of rolling passes on the microstructures and mechanical properties of Mg-Gd-Y-Zr alloy sheets, *Mater. Sci. Eng. A* 618 (2014) 232-237.
41. A. Chapuis, J.H. Driver, Temperature dependency of slip and twinning in plane strain compressed magnesium single crystals, *Acta Mater.* 59 (2011) 1986-1994.
42. Z.Y. Xue, Y.J. Ren, W.B. Luo, R.P. Zheng, C. Xu, Effect of aging treatment on the precipitation behavior and mechanical properties of Mg-9Gd-3Y-1.5Zn-0.5Zr alloy, *J. Mater. Eng. Perform.* 26 (2017) 5963-5972.
43. X.L. Hou, Z.Y. Cao, L.D. Wang, S.W. Xu, S. Kamado, L.M. Wang, Microstructure and mechanical properties of extruded Mg-8Gd-2Y-1Nd-0.3Zn-0.6Zr alloy, *Mater. Sci. Eng. A* 528 (2011) 7805-7810.
44. K. Guan, B.S. Li, Q. Yang, X. Qiu, Z. Tian, D.D. Zhang, D.P. Zhang, X.D. Niu, W. Sun, X.J. Liu, J. Meng, Effects of 1.5 wt.% samarium (Sm) addition on microstructures and tensile properties of a Mg-6.0Zn-0.5Zr alloy, *J. Alloys Compd.* 735 (2018) 1737-1749.
45. K. Hagihara, A. Kinoshita, Y. Sugino, M. Yamasaki, Y. Kawamura, H.Y. Yasuda, Y. Umakoshi, Effect of long-period stacking ordered phase on mechanical properties of Mg₉₇Zn₁Y₂ extruded alloy, *Acta Mater.* 58 (2010) 6282-6293.
46. F. Bu, Q. Yang, K. Guan, X. Qiu, D. Zhang, W. Sun, T. Zheng, X. Cui, S. Sun, Z. Tang, X. Liu, J. Meng, Study on the mutual effect of La and Gd on microstructure and mechanical properties of Mg-Al-Zn extruded alloy, *J. Alloys Compd.* 688 (2016) 1241-1250.
47. W. Yuan, S.K. Panigrahi, J. Su, R. Mishra, Influence of grain size and texture on Hall-Petch relationship for a magnesium alloy, *Scr. Mater.* 65 (2011) 994-997.
48. P. Zhang, B. Watzinger, Q. Kong, W. Blum, Microstructural evolution during creep of the Mg-Al-Alloy AZ91hp, *Key Eng. Mater.* 171-174 (2000) 609-616.
49. H.S. Jiang, X.G. Qiao, C. Xu, M.Y. Zheng, K. Wu, S. Kamado, Ultrahigh strength as-extruded Mg-10.3Zn-6.4Y-0.4Zr-0.5Ca alloy containing W phase, *Mater. Des.* 108 (2016) 391-399.
50. J.D. Robson, C. Paa-Rai, The interaction of grain refinement and ageing in magnesium-zinc-zirconium (ZK) alloys, *Acta Mater.* 95 (2015) 10e19.
51. C.R. Hutchinson, J.F. Nie, S. Gorsse, Modeling the precipitation processes and strengthening mechanisms in a Mg-Al-(Zn) AZ91 alloy, *Metall. Mater. Trans. A* 36 (2005) 2093e2105.

52. J.F. Nie, Effects of precipitate shape and orientation on dispersion strengthening in magnesium alloys, *Scr. Mater.* 48 (2003) 1009-1015.
53. K. Liu, J.H. Zhang, L.L. Rokhlin, F.M. Elkin, D.X. Tang, J. Meng, Microstructures and mechanical properties of extruded Mg-8Gd-0.4Zr alloys containing Zn, *Mater. Sci. Eng. A* 505 (2009) 13-19.